Proceedings of the ASME 2024 19th International Manufacturing Science and Engineering Conference
MSEC2024
June 17-21, 2024, Knoxville, Tennessee

MSEC2024-125486

DYNAMIC GEOMETRIC MODELING FOR DIRECTED ENERGY DEPOSITION PROCESS

Wenze Zhang[1,4], Siqi Chen[1], Boge Dong[1],
Yuanzhi Chen[2,4], Xiaoke Deng[1,4], Molong Duan[1,2,3,*], Kai Tang[2,3,4,*]

[1]The Hong Kong University of Science and Technology, Hong Kong SAR, China
[2]The Hong Kong University of Science and Technology (Guangzhou), Guangzhou, China
[3]HKUST Shenzhen-Hong Kong Collaborative Innovation Research Institute, Futian, Shenzhen, China
[4]The Hong Kong University of Science and Technology Shenzhen Research Institute, Shenzhen, China

ABSTRACT

Directed energy deposition (DED) is a prominent additive manufacturing technology for manufacturing metal parts. High-fidelity simulation can reconstruct the DED process but is typically too computationally complex for process control and planning. On the other hand, experimental-based models typically only consider the static relationship between the printed bead geometry and the printing parameters, leading to significant geometry deviations. To address this issue, we propose a dynamic model that correlates the printing parameters, such as energy deposition rate and energy moving speed, with the printed geometry, such as the width and height of the printed bead. A mirrored sigmoid model was developed to fit the geometry profile of the printed bead, and a nonlinear time-invariant system was constructed to simulate the extracted geometry. This system comprises a nonlinear static model and a linear time-invariant system that respectively handles the static relationship and the high-frequency dynamic signal increments decomposed from the whole input signals. Experimental results have verified the effectiveness of the proposed method in predicting the dynamic printed bead geometry and reducing geometry deviations.

Keywords: directed energy deposition, dynamic model, nonlinear time-invariant system.

1. INTRODUCTION

The directed energy deposition (DED) process is one of the most common methods in metal alloy additive manufacturing (AM) due to its flexibility and efficiency [1]. In a DED process, the feedstocks (e.g., metal powder) are deposited onto the substrate and heated by the directed energy (e.g., laser or electron beams). After removing the energy source, the heated feedstocks cool down and are conveyed to the cladding. The geometry of the cladding directly affects the final shape of the printed part. Therefore, the mathematical relationship between the printing parameters (such as the laser power and energy moving speed) and the cladding geometry (such as the width and height) is crucial for the accuracy and efficiency of the DED process [2].

Various existing research aimed to establish the relationship between the deposition geometry and the DED process. Ribeiro investigated the effects of deposition strategy and stepover of adjacent deposition lines on the geometry and mechanical properties of the printed parts [3]. Vundru et al. presented a comprehensive analytical-computational model for deposition geometry prediction [4]. Li et al. discussed the mechanism of heat accumulation in the DED process that affects the height and width of the printing parts [5]. Artificial intelligence (AI) algorithms and data-driven methods have also been employed in building prediction models. Menon et al. built a model that combined analytical and data-driven methods for melt pool geometry predictions [6]. Jamnikar et al. trained a convolutional neural network that predicts molten pool geometry parameters by using real-time melting pool thermal images [7]. However, the current research is concentrated on the static model and lacks ability to accurately describe the nonlinear coupling relationship between the printing parameters and the dynamic features of the DED process.

The DED process can be regarded as a multi-input-multi-output (MIMO) system, which is characterized by complex nonlinear and dynamic relationships. To decrease the deviations in geometry describing the DED process, this paper establishes a MIMO dynamic geometry model based on the analysis of the

* Corresponding author: duan@ust.hk, mektang@ust.hk

statistical data. In particular, the proposed modeling method includes the following two major contributions:

- A mirrored sigmoid profile is proposed to describe the deposition geometry of the DED process.
- A nonlinear time-invariant (NLTI) model for simulating the DED process is constructed, which consists of a nonlinear static relationship that deals with low-frequency static signals, and a linear time-invariant (LTI) dynamic system that deals with high-frequency dynamics.

The remainder of the paper is as follows: Section 2 introduces the geometry extraction method. Section 3 illustrates the process of building an NLTI model to simulate the printed geometry of the DED process. And finally, Section 4 reports the experiments and verifies the proposed model.

2. Geometry description of the printing bead

The deposited bead is scanned by a structured-light 3D camera, and a point set $P_s = (x_s, y_s, z_s)$ representing its surface geometry is collected, as shown in Figure 1.

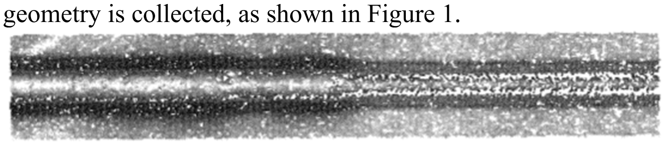

Figure 1 The point cloud scanned by the structured-light camera.

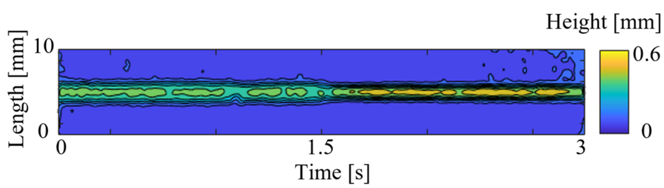

Figure 2 The mesh contour converted to reflect the printing time.

The geometry profile along the deposition direction with respect to time is extracted, following the method by Duan et al. [8], [9]. The extracted manifold is shown in Figure 2, in which P_s is used to create a mesh. At each time instance t of the printing process, the corresponding geometry profile (i.e., the cross-section pattern of the mesh) is extracted, as shown in Figure 3, which is described by a sequenced 2D point set $(u, \tilde{h}(u))$.

To fit each cross-section pattern, a sigmoid function $\sigma(u)$ is introduced as

$$\sigma(u) = \frac{1}{1+e^{-u}}. \tag{1}$$

Considering the symmetry of the geometry profile, a mirrored sigmoid profile $\hat{h} = f(u)$ is defined with the symmetry axis $u = \omega$ as:

$$\hat{h} = \begin{cases} a\sigma\left(b(u-c)\right) & (u \le \omega) \\ a\sigma\left(b((2\omega-u)-c)\right) & (u > \omega) \end{cases}, \tag{2}$$

where $\hat{h}$ is the fitted height; and a, b, and c are the scaling, stretching, and shifting parameters, respectively. Note that ω is extracted as the deposition center position. a_0, b_0, c_0, and ω_0 are defined as the parameters of the best fitting curve at the corresponding time. They are calculated by minimizing the fitting error, i.e.,

$$[a_0, b_0, c_0, d_0] = \arg\min\left(\left|\tilde{h}(u) - \hat{h}(u)\right|\right). \tag{3}$$

With the mirrored sigmoid profile, each cross-sectional shape of the printed bead is fitted very well as shown in Figure 3. But for simplification, the width and height of the bead is used to describe the geometry. The width w_0 of the geometry profile can be considered as the width of the part that is higher than the substrate by 0.01 mm, which can be calculated as

$$w_0 = 2\left|\omega_0 - \hat{h}^{-1}(0.01)\right|. \tag{4}$$

The height h_0 of the geometry profile can be represented by c_0, i.e., $h_0 = c_0$. Thus, the output of the geometry model is decided to be the width and height, i.e., $w = w(t)$ and $h = h(t)$. Figure 4 shows an example of the extracted width and height of some printed bead.

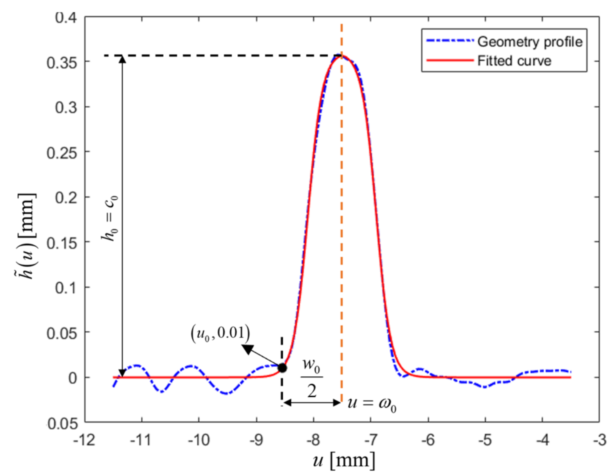

Figure 3 The extracted profile and corresponding fitting curve at a specific sample time.

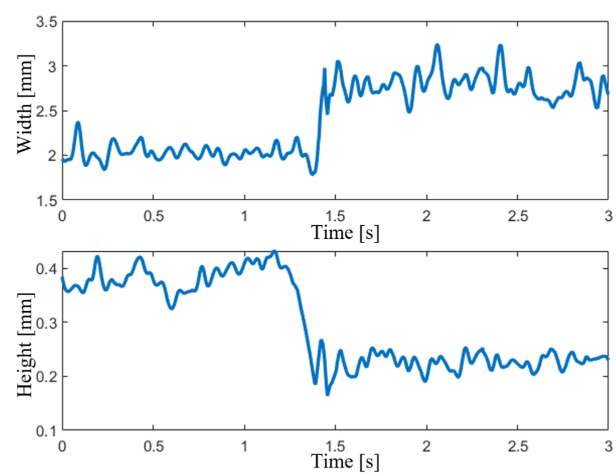

Figure 4 The extracted width and height of a printed bead.

3. NLTI modeling framework

The printing system operates as a MIMO system, where both the energy deposition rate (EDR) $p_v = p_v(t)$ and energy moving speed (EMS) $v = v(t)$ act as the dual inputs $u = [p_v, v]^\top$. Additionally, the width $w = w(t)$ and height $h = h(t)$ of the printing bead are designated as the output $y = [w, h]^\top$.

In production practice, a MIMO system of this nature is typically recognized as a nonlinear system. For simplification, the input signal u can be categorized into two components: one representing the static aspect of the signal u_l, which remains constant, and the other embodying high-frequency fluctuations Δu_h. Thus, the whole NLTI system can be deconstructed into a static nonlinear system and a dynamic linear time-invariant (LTI) system. The static nonlinear system handles u_l, and generates the static portion of the output y_l, while the dynamic LTI system manages Δu_h and generates the high-frequency variations Δy_h. Defining the output of the MIMO system to be $y = [w, h]^\top$, as shown in Equation (5).

$$\begin{aligned} u &= u_l + \Delta u_h, \\ y &= y_l + \Delta y_h. \end{aligned} \tag{5}$$

For the static part, the static nonlinear system is defined as

$$\begin{aligned} \dot{x}_l &= A_l x_l + B_l u_l, \\ y_l &= C_l x_l, \end{aligned} \tag{6}$$

where A_l, B_l, C_l are state space matrices. But the nonlinear relationships between the input and the output need to be described by nonlinear functions, which can be fitted through static experiments. With the nonlinear mapping relations $f_l : \mathbb{R}^2 \to \mathbb{R}^2$, Eq. (6) is equal to

$$y_l = f_l(u_l). \tag{7}$$

More specifically, two nonlinear functions $f_{l1} : \mathbb{R}^2 \to \mathbb{R}^1$ and $f_{l2} : \mathbb{R}^2 \to \mathbb{R}^1$ are used to calculate the width and height from the input, as

$$\begin{bmatrix} w_l \\ h_l \end{bmatrix} = \begin{bmatrix} f_{l1}(p_v, v) \\ f_{l2}(p_v, v) \end{bmatrix}. \tag{8}$$

For the dynamic part, the LTI system is used to describe the high-frequency variations:

$$\begin{aligned} \Delta\dot{x}_h &= A_h \Delta x_h + B_h \Delta u_h, \\ \Delta y_h &= C_h \Delta x_h, \end{aligned} \tag{9}$$

where A_h, B_h, C_h serve as state space matrices. More specifically, the variations of the width (or height) can be calculated as the sum of the width (or height) variations caused by the variations of the EDR and the EMS, as the following

$$\Delta y_h = \begin{bmatrix} \Delta w_h(s) \\ \Delta h_h(s) \end{bmatrix} = \begin{bmatrix} G_{p-w}(s) & G_{v-w}(s) \\ G_{p-h}(s) & G_{v-h}(s) \end{bmatrix} \begin{bmatrix} \Delta p_h(s) \\ \Delta v_h(s) \end{bmatrix}, \tag{10}$$

where G_{p-w}, G_{v-w}, G_{p-h} ,and G_{v-h} are transfer functions of the corresponding single-input-single-output (SISO) system, and s is the Laplace variable.

To sum up, the NLTI system can be described as

$$\begin{aligned} \begin{bmatrix} \dot{x}_l \\ \Delta\dot{x}_h \end{bmatrix} &= \begin{bmatrix} A_l & 0 \\ 0 & A_h \end{bmatrix} \begin{bmatrix} x_l \\ \Delta x_h \end{bmatrix} + \begin{bmatrix} B_l & 0 \\ 0 & B_h \end{bmatrix} \begin{bmatrix} u_l \\ \Delta u_h \end{bmatrix}, \\ y &= \begin{bmatrix} C_l & C_h \end{bmatrix} \begin{bmatrix} x_l \\ \Delta x_h \end{bmatrix}. \end{aligned} \tag{11}$$

Furthermore, the output width and height can be easily described by the input EDR and EMS as:

$$\begin{bmatrix} w \\ h \end{bmatrix} = \begin{bmatrix} f_{l1}(p_v, v) \\ f_{l2}(p_v, v) \end{bmatrix} + \begin{bmatrix} G_{p-w}(s) & G_{v-w}(s) \\ G_{p-h}(s) & G_{v-h}(s) \end{bmatrix} \begin{bmatrix} \Delta p_h(s) \\ \Delta v_h(s) \end{bmatrix}. \tag{12}$$

4. Experiments

To verify the effectiveness of the proposed modeling approach, bead printing experiments are conducted to construct the MIMO system, as well as to validate the model.

4.1 Experiment setup

Figure 5 shows the setup of the DED printing system and Table 1 lists its specification parameters. It consists of a five-axis machine tool as the moving platform (provided by *Jia Tie*), a laser as the energy source and a powder feeder (provided by *Hui Rui*). Argon is employed in the printing system as the shielding gas. Any modifications to the printing parameters can significantly impact the final shape. Therefore, the following key settings remain unchanged throughout the printing to ensure consistency and accuracy in the results, as given in Table 1.

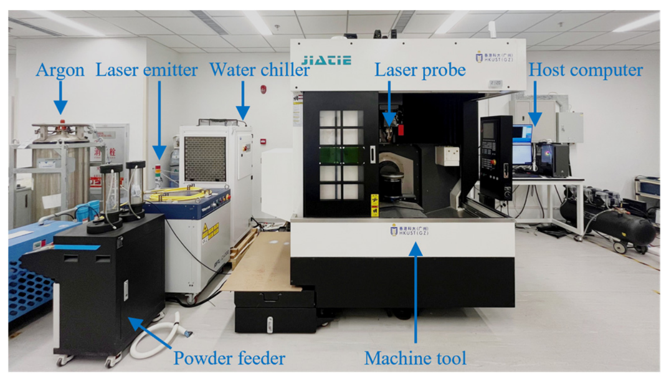

Figure 5 The homebuilt DED printing system.

Table 1 Printing Parameters

Maximum print volume	500×500×500 mm^3
Maximum acceleration	1000 mm/s^2
Laser wavelength	1064 nm
Laser spot size	2 mm
Powder material	316L stainless steel
Powder diameter	70~150 μm
Powder feed rate	9.4 g/min
Gas flow	5 L/min
Gas pressure	1.5 MPa

As shown in Figure 6, a structured light camera is employed to measure the geometry of the part in printing. The camera utilizes structured light technology to capture and measure the depth information. The underlying principle for obtaining a point cloud from this camera involves projecting a pattern of structured light onto the objects and subsequently capturing the deformed pattern using a camera sensor [11]. The configuration parameters of the structured light camera are given in Table 2.

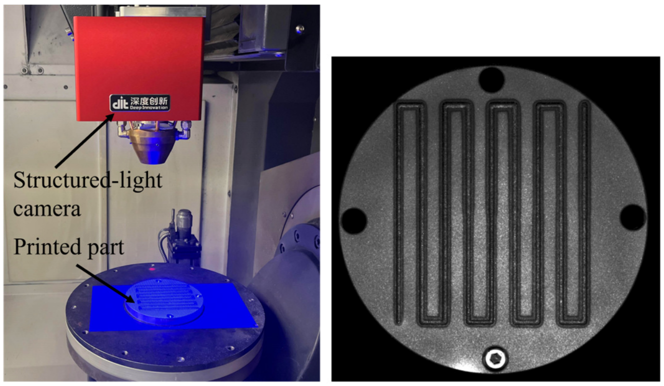

(a) (b)

Figure 6 The measurement system: (a) the structured light camera setup, and (b) the collected cloud points.

Table 2 Structured light camera specification.

Brand	Deep Innovation
Type	M05G016-230
Depth of focus	200~260 mm
Horizon	160×100 mm
Measurement precision	0.01 mm
Measurement repetition precision	0.005 mm

4.2 Trajectory generation for printing parameter generation

To enhance the system identification process, it is crucial for the machine to accurately execute the input parameters, i.e., the energy deposition rate (EDR) and the energy moving speed (EMS). Both are programmed into the G-codes which are transmitted to the machine. The laser emitter has the capability to adjust the laser power within 10 µs, allowing EDR change to be considered as a step signal. As for the EMS, the machine tool will further interpolate and smooth it to minimize the impact load of variable speed. Therefore, it is imperative to utilize incremental short G-codes to precisely control the EMS. The incremental step length for G-codes is 0.005 mm in this paper.
As shown in Figure 7, for the variable speed section, a trapezoidal velocity planning with a constant acceleration of 100 mm/s^2 is employed. Subsequently, the trapezoidal velocity planning result is smoothed using an average convolution smoother, with the following transfer function:

$$H(Z)=\frac{1}{N}\left(1+z^{-1}+z^{-2}+\ldots+z^{-(N-1)}\right). \tag{13}$$

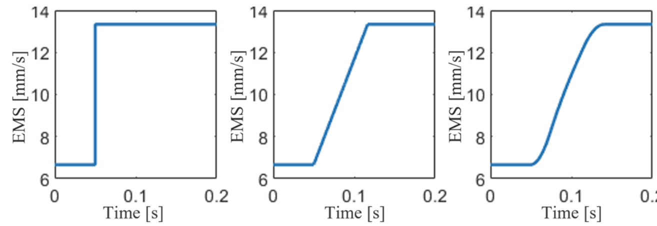

(a) (b) (c)

Figure 7 The energy moving speed curve: (a) original energy moving speed step, (b) trapezoidal velocity planning results, and (c) average convolution smoother results.

4.3 Static modeling

The proposed model takes the energy moving speed (EMS) $v(t)$ and the energy deposition rate (EDR) $p_v(t)$ into consideration. To avoid the uncoated defects in the DED process, trial and error tests are conducted to find the proper parameter range. The final ranges of $v(t)$ and $p_v(t)$ are set from 6.67 mm/s to 13.33 mm/s and 50 J/mm to 150 J/mm, respectively. The trajectory in Figure 8 are printed five times with the energy deposition rate in 50, 75 100, 125, 150 J/mm for static geometry response identification. For each time, the experiment trajectories are shown in Figure 8 with varying energy moving speed $v(t)$. After printing, the mirrored sigmoid profiles are extracted, and a nonlinear function is fitted to describe the correlations. The extracted static width and height of the corresponding response are shown in Table 3 and Table 4. And the consequently generated static response surface models (RSM) are shown in Figure 9. The nonlinear function of the steady-state response is:

$$\varsigma = p_{00}+p_{10}p+p_{01}v+p_{20}p^2+p_{11}pv+p_{02}v^2+p_{30}p^3+ \\ p_{21}p^2v+p_{12}pv^2+p_{03}v^3, \tag{14}$$

where ζ is the fitted result geometry parameter.

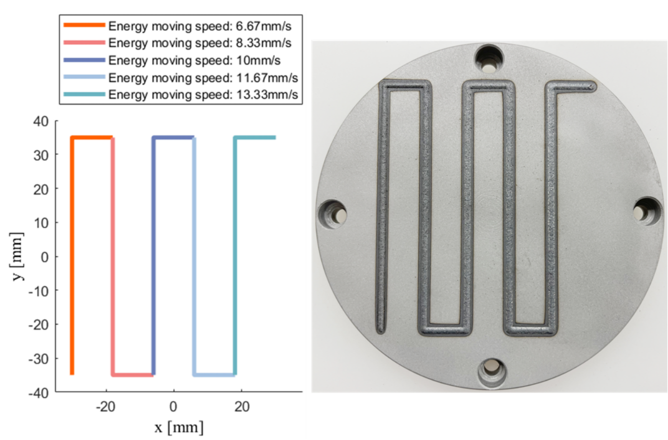

(a) (b)

Figure 8 Experimental trajectories and results: (a) the trajectory for static geometry response identification (the EDR is respectively set to 50, 75, 100, 125, 150 J/mm), and (b) the corresponding printed results.

Table 3 The extracted static width (mean value ± standard deviation, unit: mm)

EDS (mm/s) / EDR (J/mm)	6.67	8.33	10	11.67	13.33
50	1.3543 ± 0.0110	1.0678 ± 0.0439	1.4073 ± 0.0066	1.4228 ± 0.0070	1.3820 ± 0.0095
75	2.2045 ± 0.0075	2.1511 ± 0.0042	2.2331 ± 0.0040	2.2784 ± 0.0100	2.2276 ± 0.0055
100	2.8032 ± 0.0034	2.9485 ± 0.0083	2.8412 ± 0.0041	2.9245 ± 0.0066	2.9332 ± 0.0080
125	3.0077 ± 0.0056	3.1943 ± 0.0047	3.1307 ± 0.0059	3.0198 ± 0.0048	3.1964 ± 0.0080
150	3.2786 ± 0.0043	3.1582 ± 0.0092	3.1344 ± 0.0045	3.3634 ± 0.0081	3.3519 ± 0.0171

Table 4 The extracted static height (mean value ± standard deviation, unit: mm)

EDS (mm/s) / EDR (J/mm)	6.67	8.33	10	11.67	13.33
50	0.2434 ± 0.0107	0.0992 ± 0.0180	0.2180 ± 0.0055	0.1693 ± 0.0082	0.1879 ± 0.0062
75	0.4049 ± 0.0053	0.3019 ± 0.0041	0.3102 ± 0.0277	0.2613 ± 0.0050	0.2376 ± 0.0103
100	0.4271 ± 0.0084	0.3527 ± 0.0084	0.3280 ± 0.0104	0.2997 ± 0.0045	0.2479 ± 0.0026
125	0.4686 ± 0.0102	0.3944 ± 0.0236	0.3471 ± 0.0057	0.3261 ± 0.3126	0.3126 ± 0.0235
150	0.4971 ± 0.0042	0.4387 ± 0.0150	0.3796 ± 0.0052	0.3427 ± 0.0075	0.2937 ± 0.0150

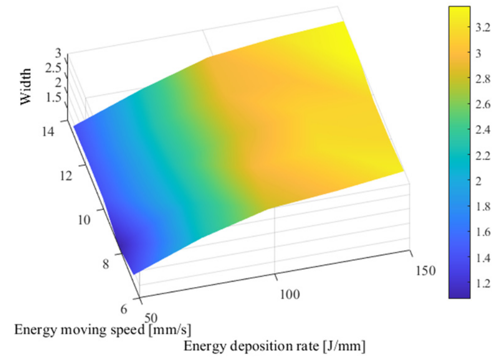

(a)

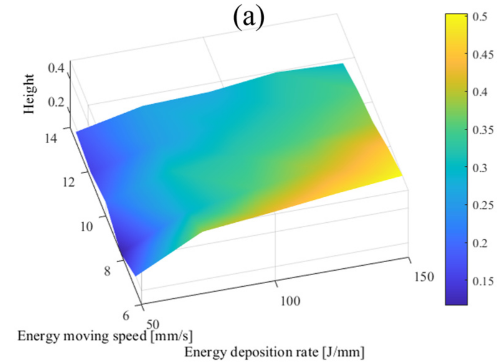

(b)

Figure 9 The static RSM with the energy feed rate and energy deposition rate: (a) for the width, and (b) for the height.

4.4 Dynamic modeling

After establishing the static model, the dynamic model of the printing geometry is identified. The trajectories in Figure 10 and Figure 11 are used for system identification. As the system is assumed to be linear, the response to the change of EDR and EMS is identified separately. The trajectory used for system identification in the energy deposition rate involves a step reduction in energy deposition rate $p(t)$ from 100 J/mm to 60 J/mm, while the EMS $v(t)$ remains constant at 10 mm/s, as shown in Figure 10. The identification in the energy moving speed $v(t)$ involves a quasi-step reduction from 13.33 mm/s to 6.66 mm/s, while $p(t)$ is held constant at 80 J/mm, as shown in Figure 11. The geometry profiles of the corresponding printed parts are collected and are used for the ensuing transfer function estimation.

The dynamic responses of the width and height under high-frequency signal increments of the input are separately analyzed. From Figure 12 (a) and (b), EDR has a dynamic incremental signal, but EMS keeps static. Figure 12 (c) and (d) illustrate the width and height responses respectively, as well as the simulation results generated from the estimated transfer functions $G_{p-w}(s)$

and $G_{v-w}(s)$ in Equation. (10). Meanwhile, $G_{p-h}(s)$ and $G_{v-h}(s)$ are also estimated from Figure 13.

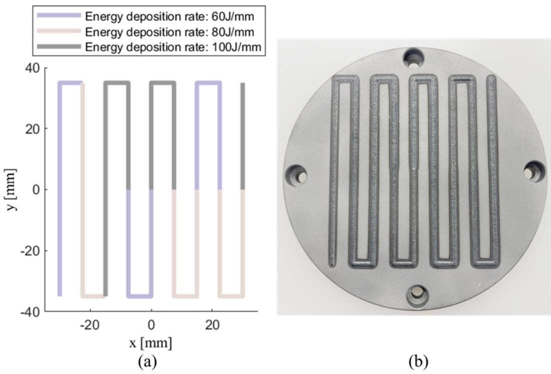

Figure 10 Dynamic system identification experiments for the input EDR: (a) the trajectory, and (b) the corresponding printed results.

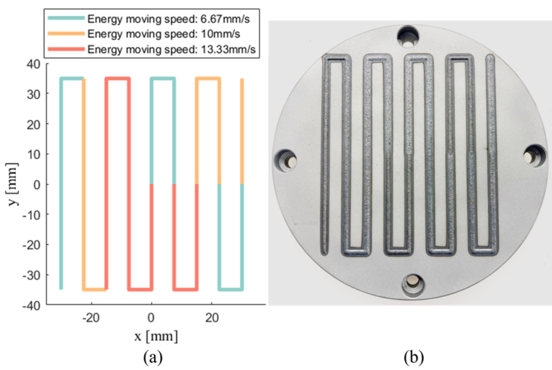

5

Figure 11 Dynamic system identification experiments for the input EMS: (a) the trajectory, and (b) the corresponding printed results.

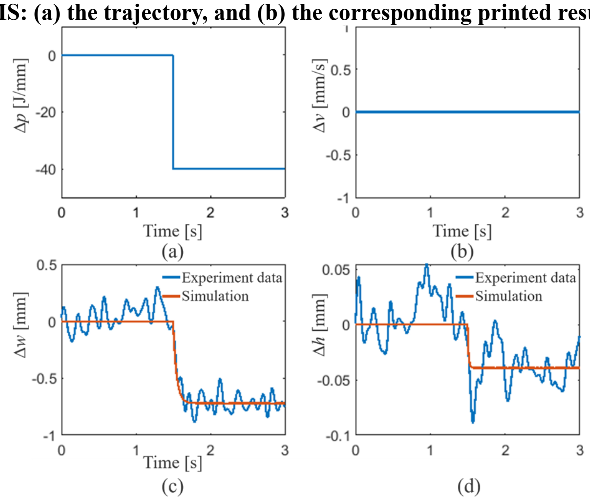

Figure 12 The dynamic response of the width and height corresponding to dynamic incremental signals of EDR: (a) step signal of EDR, (b) static EMS signal, (c) width response, and (d) height response.

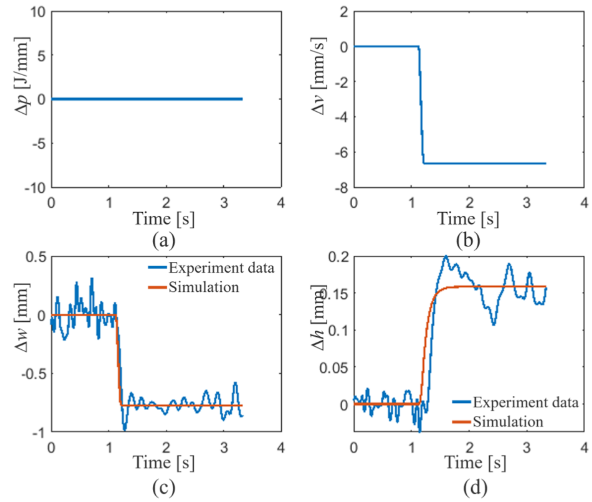

Figure 13 The dynamic response of the width and height corresponding to dynamic incremental signals of EMS: (a) static EDR signal, (b) quasi-step signal of EMS, (c) width response, and (d) height response.

4.5 Verification of the NLTI system

Now that the fitted model for the static input and the transfer functions for the high-frequency dynamic input variations are generated, the whole NLTI system can be described.

For verifying the NLTI system, it is designed that the two printing parameters changed simultaneously, i.e., EDR changed from 100 to 60 J/mm and the EMS changed from 13.33 to 6.67 mm/s. Although the input changed at the same time, the end time is different. Because the EDR change can be seen as a step response, but the EMS change needs a S-shaped speed plan process. The input is divided into the low-frequency and high frequency signals with the first difference transformation method, as shown in Figure 14. The top row in Figure 14 is the original input, while the middle and bottom rows are the decomposed low-frequency static signal and high-frequency dynamic signal, respectively.

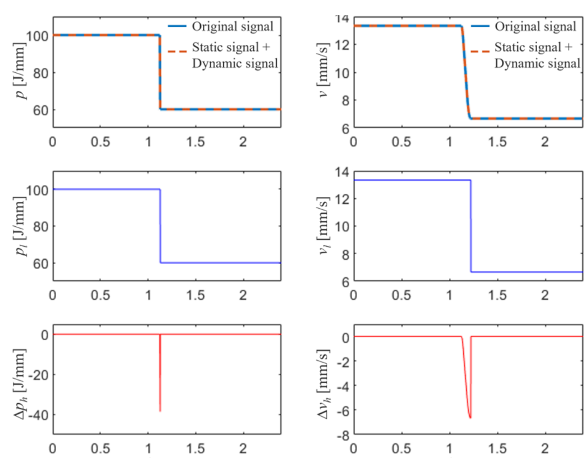

Figure 14 Signal separation based on frequency.

With the separated signal, the response of height and width corresponding to the static (the top row in Figure 15) and dynamic incremental (the bottom row in Figure 15) signals are calculated separately based on the corresponding models.

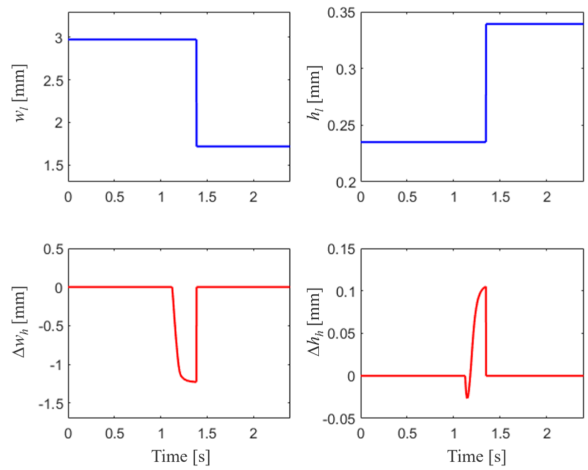

Figure 15 Responses of the width and height corresponding to different signals.

The sum of the static and the dynamic incremental responses is the total response of the NLTI system. To prove the effectiveness of the proposed method, the static non-linear model generated in Figure 9 is compared. Figure 16 shows the experiment data and the simulation results of the two methods. Compared to the simulation result from the static non-linear model, the proposed method's result is more accurate as it considers dynamic characteristics. The simulation results from the proposed approach closely match the real situation, indicating that the proposed method is effective.

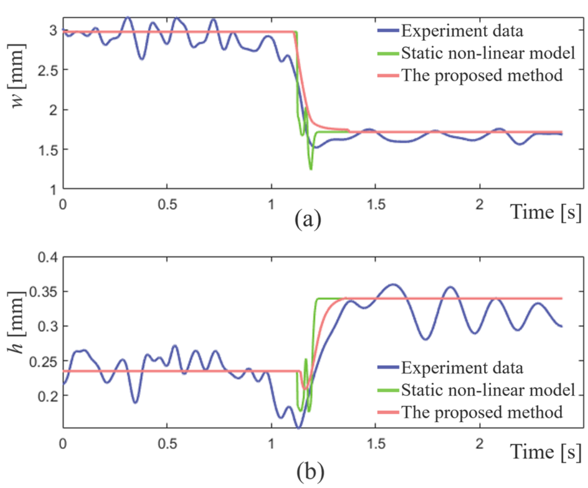

Figure 16 Comparison between the total response of the NLTI system and the experiment data: (a) for width, and (b) for height.

5. CONCLUSION AND FUTURE WORK

This paper built a dynamic model describing the correlation between the geometry of the DED process and the printing parameter inputs. A mirrored sigmoid profile is proposed to fit the geometry of the deposited path. Based on it, the width and height of the geometry profile are defined to represent the geometry of the DED process. With the energy deposition rate and energy moving speed serving as the input, a nonlinear time-invariant (NLTI) system is constructed to simulate the dynamic responses of the geometry (i.e., the width and height of the deposited bead). This system decomposes the dynamic input signal into low-frequency static signals and high-frequency dynamic signal increments. The former one is handled by a nonlinear static model, and the latter is processed by an LTI dynamic system. The sum of both responses constitutes the final response of the NLTI system. The proposed NLTI modeling of the dynamic DED process is verified in experiments wherein the deposition energy and speed are simultaneously varied.

In the future, the dynamic model will be extended to describe the curved and corner shapes, as well as multi-layer objects in DED printing.

ACKNOWLEDGEMENTS

The authors acknowledge support from the HKUST Bridge Gap Fund (BGF) and HKUST-HKUST(GZ) 20 for 20 Cross-campus Collaborative Research Scheme. This work was supported in part by (1) Foshan HKUST Projects (Project ID: FSUST20-SRI09E); and (2) the Project of Hetao Shenzhen-Hong Kong Science and Technology Innovation Cooperation Zone (HZQB-KCZYB-2020083). Profs. Pengcheng Hu and Dong He provided valuable feedback to this work. The help from the funding agency and the other researchers is sincerely appreciated.

REFERENCES

[1] M. Lalegani Dezaki *et al.*, "A review on additive/subtractive hybrid manufacturing of directed energy deposition (DED) process," *Adv. Powder Mater.*, vol. 1, no. 4, p. 100054, 2022, doi: 10.1016/j.apmate.2022.100054.

[2] U. de Oliveira, V. Ocelík, and J. T. M. De Hosson, "Analysis of coaxial laser cladding processing conditions," *Surf. Coatings Technol.*, vol. 197, no. 2–3, pp. 127–136, 2005, doi: 10.1016/j.surfcoat.2004.06.029.

[3] K. S. B. Ribeiro, F. E. Mariani, and R. T. Coelho, "A Study of Different Deposition Strategies in Direct Energy Deposition (DED) Processes," *Procedia Manuf.*, vol. 48, no. 2019, pp. 663–670, 2020, doi: 10.1016/j.promfg.2020.05.158.

[4] C. Vundru, R. Singh, W. Yan, and S. Karagadde, "International Journal of Mechanical Sciences A comprehensive analytical-computational model of laser directed energy deposition to predict deposition geometry and integrity for sustainable repair," *Int. J. Mech. Sci.*, vol.

211, no. May, p. 106790, 2021, doi: 10.1016/j.ijmecsci.2021.106790.

[5] G. Li, K. Odum, C. Yau, M. Soshi, and K. Yamazaki, “High productivity fluence based control of Directed Energy Deposition (DED) part geometry,” *J. Manuf. Process.*, vol. 65 February, pp. 407–417, 2021, doi: 10.1016/j.jmapro.2021.03.028.

[6] N. Menon and A. Basak, “Prediction of Melt Pool Geometry by Fusing Experimental and Simulation Data,” *Int. J. Mech. Sci.*, p. 108786, 2023, doi: 10.1016/j.ijmecsci.2023.108786.

[7] N. D. Jamnikar, S. Liu, C. Brice, and X. Zhang, “In - process comprehensive prediction of bead geometry for laser wire - feed DED system using molten pool sensing data and multi - modality CNN,” *Int. J. Adv. Manuf. Technol.*, pp. 903–917, 2022, doi: 10.1007/s00170-022-09248-3.

[8] M. Duan, S. Chen, and Y. Yang, “Thermal-image-enabled additive manufacturing process monitoring and extrusion trajectory compensation,” *Proc. ASME 2023 Manuf. Sci. Eng. Conf.*, pp. 1–10, 2023.

[9] S. Chen, Y. Yang, S. Liu, and M. Duan, “In-situ additive manufacturing deposition trajectory monitoring and compensation with thermal camera,” *Addit. Manuf.*, vol. 78, no. September, p. 103820, 2023, doi: 10.1016/j.addma.2023.103820.

[10] M. Duan, D. Yoon, and C. E. Okwudire, “A limited-preview filtered B-spline approach to tracking control – With application to vibration-induced error compensation of a 3D printer,” *Mechatronics*, vol. 56, pp. 287–296, Apr. 2018, doi: 10.1016/J.MECHATRONICS.2017.09.002.

[11] M. Rodriguez-Martin, P. Rodriguez-Gonzalvez, D. Gonzalez-Aguilera, and J. Fernandez-Hernandez, “Feasibility Study of a Structured Light System Applied to Welding Inspection Based on Articulated Coordinate Measure Machine Data,” *IEEE Sens. J.*, vol. 17, no. 13, pp. 4217–4224, 2017, doi: 10.1109/JSEN.2017.2700954.

